Electronic Supplementary Information (ESI)

Direct Bandgap Opening in Sodium-Doped Antimonene Quantum Dots: An Emerging 2D Semiconductor

Liang Hu,[a] *Zhenyu Xu,*[a] *Fangchao Long,*[a] *Jun Yuan,*[a] *Hui Li,*[a] *Ailun Zhao,*[a] *Su-Ting Han,*[b] *Nian Zhang,*[c] *Xiaosong Liu,*[c] *Chao Ma,*[d] *Shuangchen Ruan,*[*a] *Yu-Jia Zeng*[*a]

[a] College of Physics and Optoelectronic Engineering, Shenzhen University, Shenzhen 518060, P. R. China

[b] Institute of Microscale Optoelectronics, Shenzhen University, Shenzhen 518060, P. R. China

[c] State Key Laboratory of Functional Materials for Informatics, Shanghai Institute of Microsystem and Information Technology, Chinese Academy of Sciences, Shanghai 200050, P. R. China

[d] College of Materials Science and Engineering, Hunan University, Changsha 410082, P. R. China

List of Supplementary Materials

Note S1. Experimental section

1.1 Synthesis of Sb:Na QDs

The Na-doped antimonene (Sb:Na) was prepared by a well-established electrochemical exfoliation technique in the Na-containing electrolyte. Specifically, an β-Sb single crystal (99.99%, 3×5×1 mm, Nanjing MKNANO) is mounted on cathodic Pt foil through a fixture and inserted in a sealed two-electrode electrochemical cell, where sodium sulfate anhydrous (99.999%, metals basis, Aladdin) was dissolved in the deionized (DI) water as the electrolyte (0.1 M). A Pt wire was used as the anode and the distance between the anode and the cathode was fixed at 1.5 cm. By applying a DC constant voltage (5~10 V), the β-Sb single crystal was electrochemically exfoliated and synchronously doped by the Na^+ ions. Through selectively collecting super supernatant and sediment, QDs and nanosheets were step-by-step separated from each other via high-speed centrifuge with the rotational speeds from 1000 rpm (70×g) to 16000 rpm (17800×g). The precipitates from supernatants were re-dispersed in the DI water and centrifuged at 16000 rpm for 20 min five times to wash the residual electrolyte and separate monolayer Sb:Na QDs. Undoped antimonene was synthesized by milling single crystal and ultrasonicating them in the isobutanol via tip-sonicator. Purification and separation process were similar to the aforementioned procedure.

1.2 Device Fabrication and Measurements

To fabricate self-assembled films, purified Sb:Na QDs solids were dispersed in anhydrous alcohol to form a dilute colloidal solution with a concentration of ≈ 200 ppb. Then a droplet of QDs alcohol dispersion was drop-casted onto a p^{++}-Si/SiO_2 substrate (1×1 cm). Prior to the drop-casting, all substrates were thoroughly cleaned with acetone, isopropanol, and DI water, and finally treated by oxygen plasma (400 W, 30 s). By carefully blowing using a rubber suction bulb towards droplet in multiple directions, primary particulate films were formed. Then, all primary films were transferred into the vacuum oven (60°C) for a whole night, which helped to

form homogeneously stacked quasi-2D films (thickness of ≈40 nm, i.e. about 60 monolayers). Before the electrodes were fabricated, the Ar^+ plasma treatment (30 W, 20 s) for the film was applied to remove surface oxidized species and optimize the contact between film and electrodes. After that, Cr (5 nm) /Au (45 nm) contacts were defined with prepatterned metallic mask and deposited by magnetron sputtering. The electrical measurements of all FETs including transfer and output characteristics were conducted in Keysight B2902A and Keithley 4200A-SCS semiconductor analyzers in ambient atmosphere. As for the electrically-transduced Raman measurements, a droplet of 100 μL dye solution of R6G with different concentrations was first drop-casted on the channel layer of FETs. After a gentle dry process, in-situ Raman measurements were performed.

1.3 Characterizations

The atomic scale observation, size information and elemental distribution were conducted in HAADF-STEM (JEOL ARM-200F) operating at 200 kV accelerating voltage. The thickness of QDs/nanosheets were confirmed by AFM (VEECO Multimode V). Optical microscopy images and Raman spectra were recorded using a confocal μ-Raman spectrometer (WITec alpha300R, 532 nm laser excitation, a micrometer resolved XYZ scanning stage, a ×100 objective lens of NA= 0.90). In order to reduce the damage of laser irradiation, Raman tests were maintained at 1 mW. All signals were acquired for ten seconds and accumulated two times. UPS and XPS studies were carried out on an ESCALAB 250XI (Thermo Scientific) using He I (21.2 eV) and Al *K*α monochromatic source (1486.6 eV), respectively. Ar^+ etching was applied prior to the measurements. To ensure the reliability of data, the measured samples were stored under ambient condition for at least one month and remeasured. No evident spectral variations were found in the XPS and UPS spectra. XRD patterns were collected in X-ray diffractometer (Rigaku MiniFlex600) with Cu Kα radiation (λ = 1.5104 Å). The soft X-ray absorption spectroscopy (sXAS) experiments were performed at beamline 02B02 at the

Shanghai Synchrotron Radiation Facility (SSRF). The bending magnet beamline provided photons with energy range from 50 to 2000 eV. The photon flux was approximately 10^{11} photons s^{-1} and the energy resolving power was 5000 at 1100 eV. The beam size at sample was set to 150 μm×50 μm. The *K*-edge of Na spectra were collected using surface-sensitive total electron yield (TEY) at room temperature in an ultrahigh vacuum chamber with a base pressure better than 1×10^{-9} Torr. Diffuse reflectance spectra (DRS) and UV-vis-NIR absorption spectra were obtained from a PerkinElmer LAMBDA spectrophotometer. Time-resolved single-photon counting (TCSPC) data were recorded by home-built confocal FLIM microscope on an inverted optical microscope (Olympus IX71) equipped with a set of galvo scanning mirrors (Yanus IV, Till photonics, Chromaphor). Data was loaded and analyzed in the PAM software (https://pam.readthedocs.io) written in MATLAB (The MathWorks, Eindhoven, The Netherlands).

1.4 DFT calculations

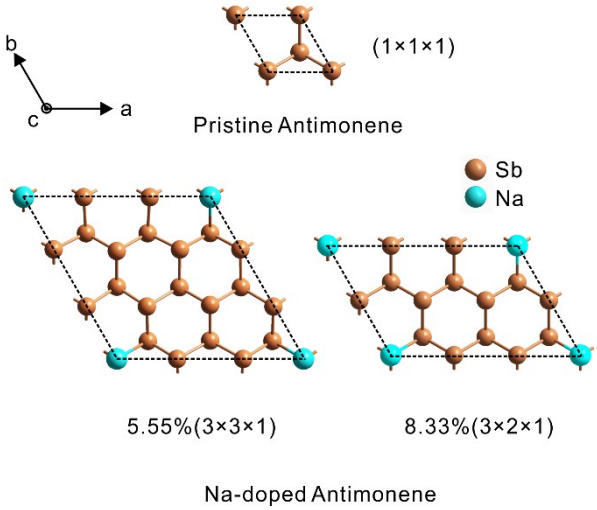

DFT calculations were performed using the Ab initio Simulation Package (VASP) code by using the screened hybrid functional of Heyd, Scuseria, and Ernzerhof (HSE06). Electron-ion interactions are treated using projector augmented wave (PAW) potentials. A Perdew-Burke-Ernzerhof (PBE) generalized gradient approximation (GGA) was used to approximate electronic exchange and correlation. All atoms were fully relaxed till the atomic Hellmann-

Feynman forces are less than 10^{-3} eV Å^{-1}. The total energy in the self-consistency process was converged to 10^{-5} eV. A vacuum layer of 15 Å was built to avoid spurious interactions. The Brillouin zone was sampled with 7×7×1 Monkhorst-Pack meshes for geometry optimization and property calculations. The plane-wave cutoff energy was 400 eV. For the primitive cell of pristine (undoped) antimonene, it belongs to the monoclinic with C2/m space group, and the lattice constants of a and b are both 4.05 Å. While considering Na-doped structures, the primitive cell of antimonene was expanded into 3×3×1 ($Sb_{17}Na_1$, a=b=11.96 Å) and 3×2×1 ($Sb_{11}Na_1$, a=12.15 Å, b=8.10 Å) supercells to meet different doping concentrations (5.55% and 8.33%), respectively. We tested the possible doping position of Na, and used the lowest energy as the calculation models. To calculate the effect of R6G adsorbates in the dilute limit, we placed a molecule on antimonene-based slabs consisting of 5×5×1 supercell. A vacuum space above 15 Å perpendicular to the slab was used to avoid the interaction of adjacent supercells. The binding energies for R6G adsorbed on these substrates including monolayer, bi-layer antimonene and monolayer Sb:Na were calculated through $E_b = E_{Sb} + E_{R6G} - E_{system}$, where E_{Sb}, E_{R6G} and E_{system} were the energies of Sb-based substrates, an R6G molecule, and the hybrid system composed of Sb-based substrate and R6G, respectively.

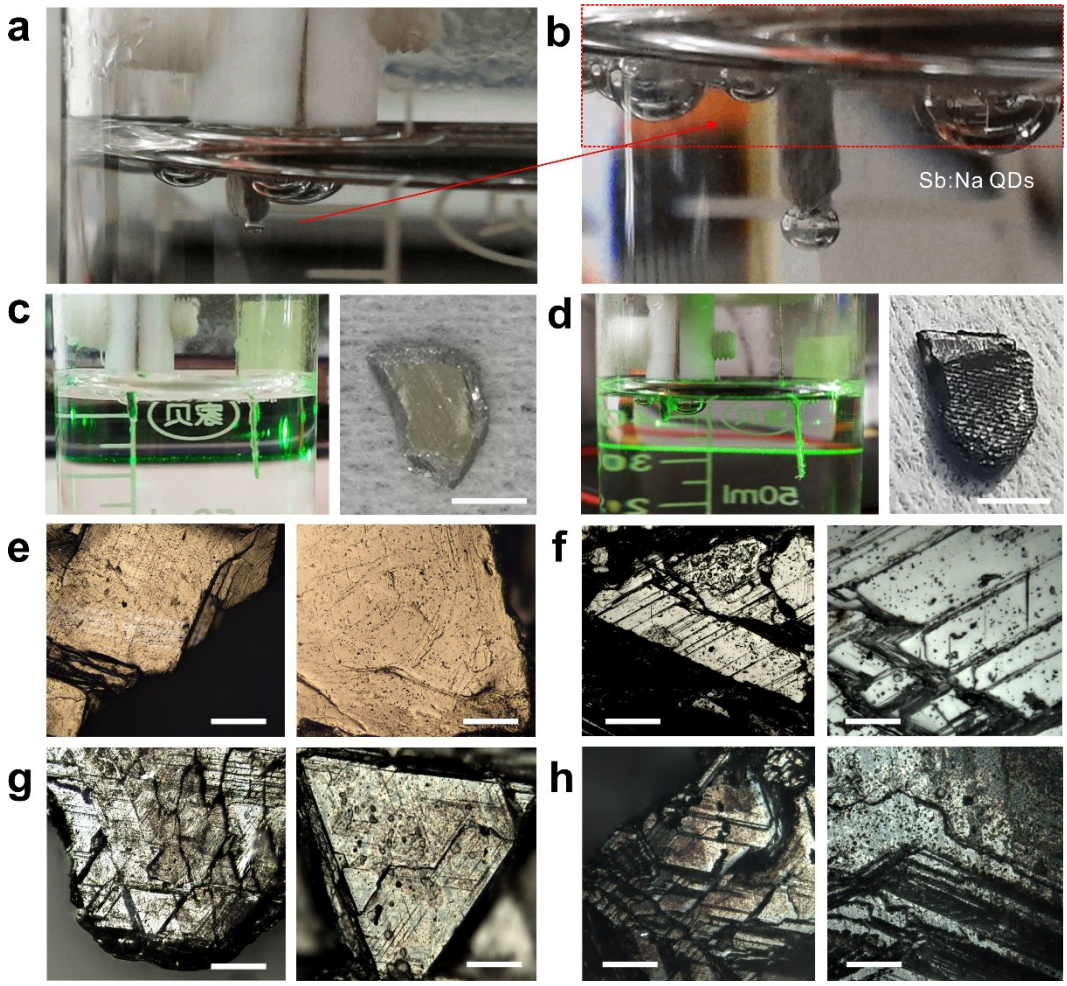

Fig. S1. Images of electrochemical exfoliation and doping process of single crystal antimony. (a-b) Cathodic intercalation of Na^+ ions. A large quantity of small fragments was exfoliated from the bulk crystal into Na_2SO_4 solution. (c-d) Electrolyte and single crystal before (c) and after (d) electrochemical exfoliation and doping. Tyndall effect is used to verify the formation of colloidal Sb nanosheets and QDs. The scale bar in (c-d) is 5 mm. (e-h) Survey and enlarged microscopic images for initial (e), mildly (f), moderately (g), and severely (h) exfoliated single crystal surfaces. It is observed that some triangle and stepped surface morphologies becomes obvious as the applied voltage increases from 6 V (mild) to 7 V (moderate) to 10 V (severe). The scale bars in (e-h) are 20 μm (for survey view) and 5 μm (for enlarged view), respectively.

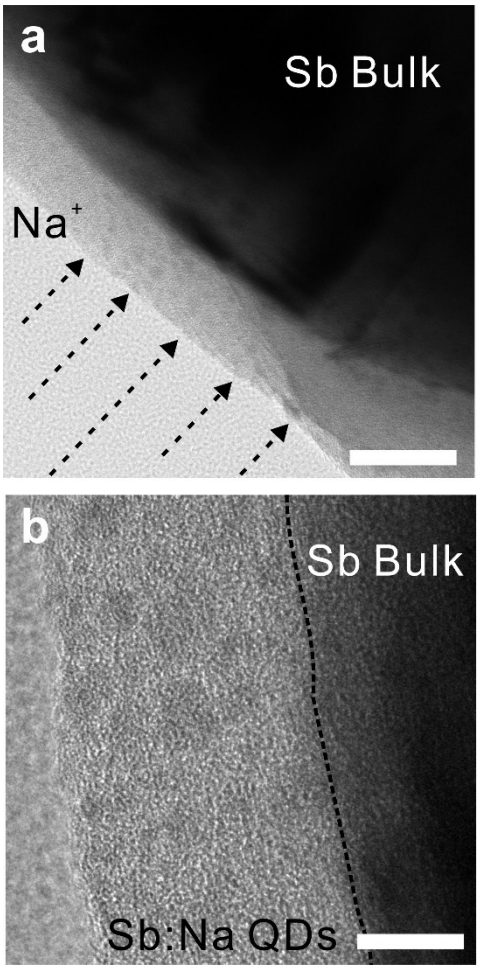

Fig. S2. TEM images of the formation process of Sb:Na QDs. (a-b) Survey (a) and enlarged (b) TEM images of intercalated surface of bulk crystal. Some tiny QDs can be found in very shallow surface area (~20 nm) when the exfoliation process first take place. The scale bars in (a) and (b) are 20 nm and 10 nm, respectively.

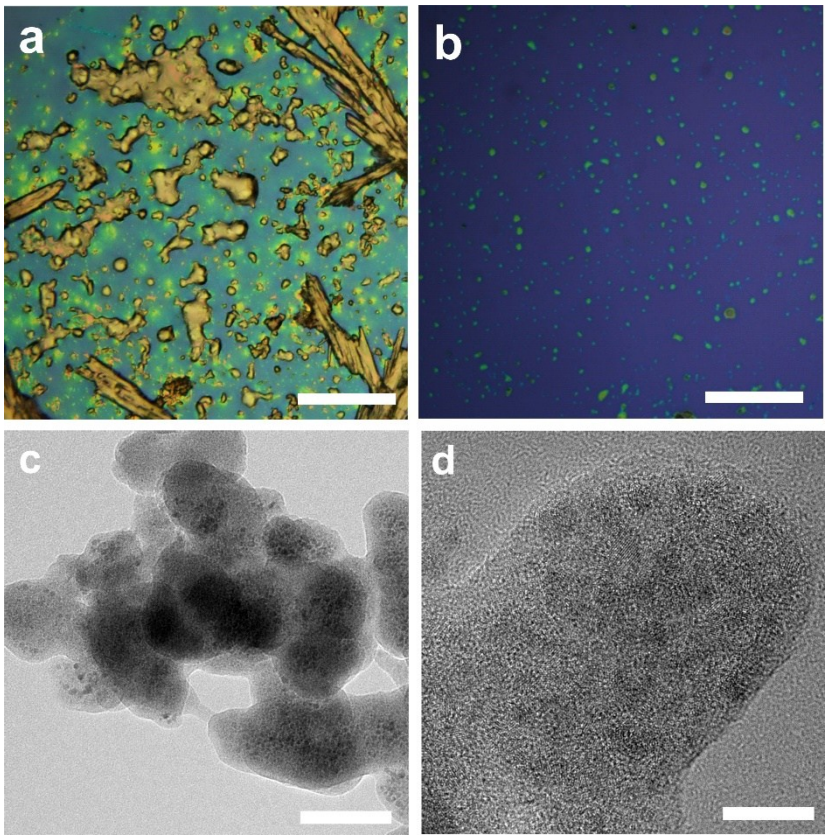

Fig. S3. Aggregated and free-standing Sb:Na QDs before (a) and after (b) residual Na^+ ions are removed from QDs. The scale bar is 10 μm. Multiple washing process is crucial for purifying QDs, size separation and post-application. (c-d) The TEM morphology of aggregated QDs for survey (c) and enlarged (d) observation. Such a case will happen when the electrolytes are not fully washed away. The scale bars in (c) and (d) are 20 nm and 10 nm, respectively.

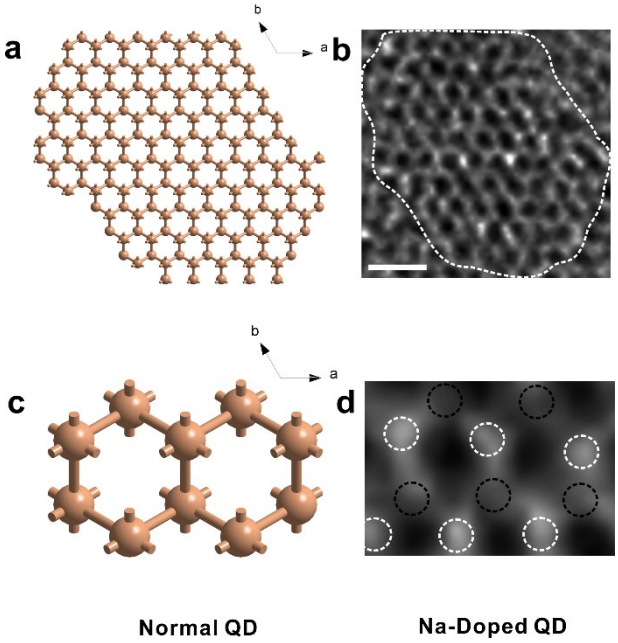

Fig. S4. The structural comparison between normal (a, c: models) and Na-doped (b, d: experimental results) antimonene QDs. Scale bar in (b) is 1 nm.

As shown in **Fig. S4 (a)**, each Sb atom of *β*-phase antimonene bonds with three adjacent Sb atoms by sp^3 hybridization, forming a buckled hexangular honeycomb atomic structure. Due to the limitation of the method in our work (top-down liquid-phase exfoliation technique rather than bottom-up molecular beam epitaxy technique), the doping of Na ions into QDs is not so controllable so that the original buckled structure might be disordered or indistinguishable in HRTEM image (**Fig. S4 (b)**). In addition, the procedure of specimen preparation for TEM measurements might unintentionally involve solvent or ions contamination, which also lead to a reduced resolution of TEM images. Even so, we can still find some twisted buckled units in such a doped honeycomb structure. As depicted in **Fig. S4 (d)**, the clear up-and-down atomic arrangement can be captured, which is indicated by white and black dotted circles, respectively, and corresponds well to the model structure in **Fig. S4 (c)**.

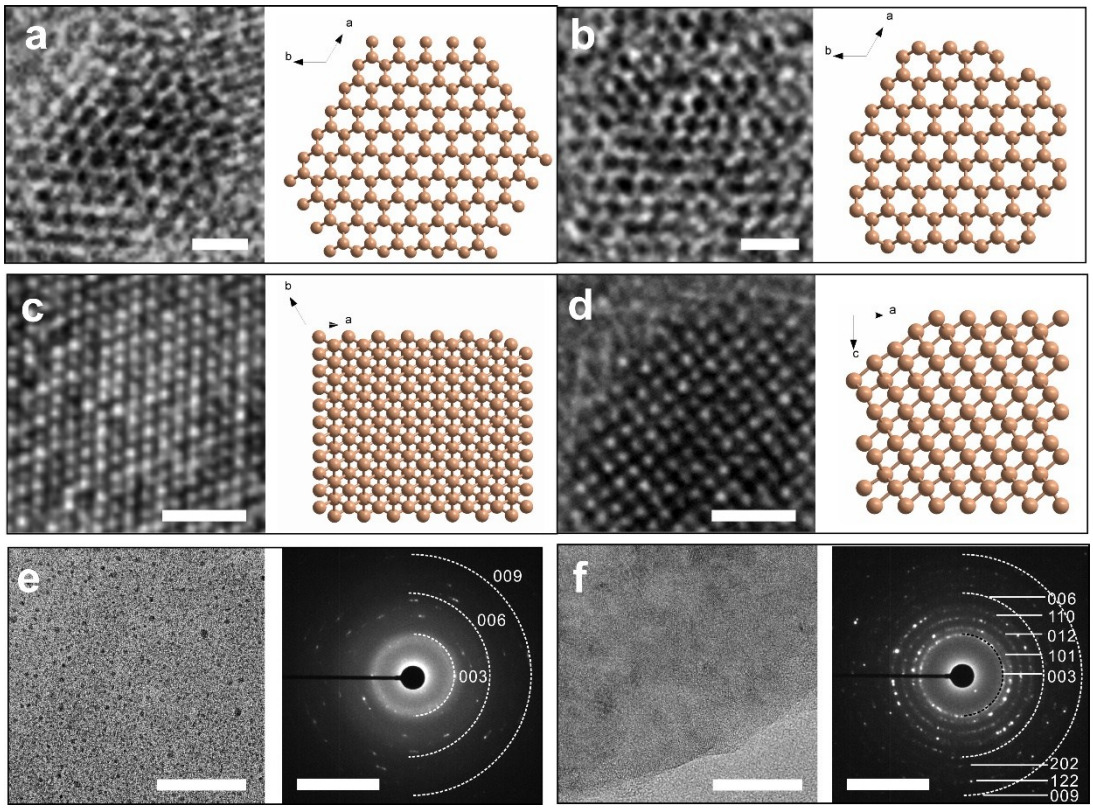

Fig. S5. TEM images and SAED patterns of Sb:Na QDs. (a-d) HRTEM images and atomic arrangement simulations for monolayer (a-b) and multi-layer Sb:Na QDs (c-d). (e-f) Survey TEM and SAED patterns of monolayer (e) and multi-layer (f) Sb:Na QDs. The scale bars in (a-d) are all 1 nm and the bars in (e-f) are both 20 nm for TEM and 5 nm^{-1} for SAED. For latter (f), due to the relatively large weight difference, a centrifugal process (> 16000 rpm) can easily separate the multi-layer Sb:Na QDs from all QDs. In contrast to the SAED pattern of the multi-layer QDs, the monolayer ones possess more incomplete diffraction rings and {003} planes can hardly be observed, which is indicative of a weakened interlayer interaction for the monolayer structure.

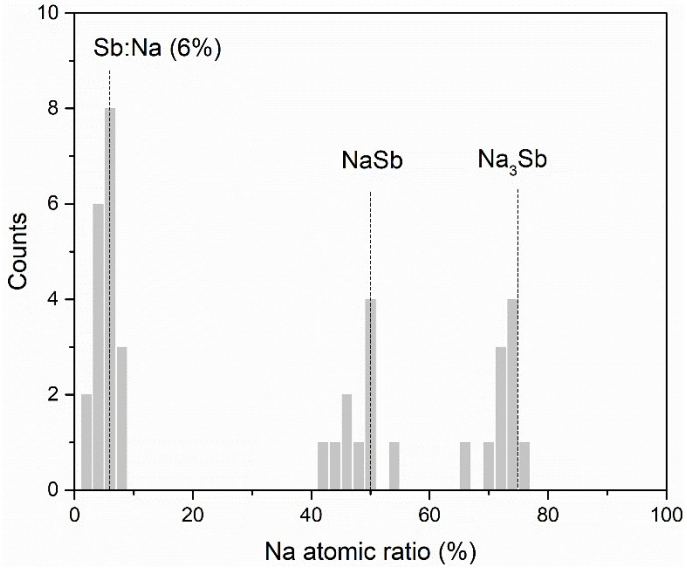

Fig. S6. The statistical histogram of Na doping ratio of the exfoliated solids in supernatant and sediment under different exfoliation voltages.

A higher electric field can drive Na^+ ions to intercalate into Sb more efficiently. For thin monolayer antimonene, the content of Na always maintains below 10% and the most favorable distribution is approximately 6%. For those thick flakes, there are two optimal doping windows, i.e. 50 % and 75 %, which corresponds to NaSb and Na_3Sb alloy phase, respectively.[1] Therefore, the doping ratio of Na in Sb can be controlled to some extent, which is close correlated to the thickness of exfoliated products. But for the monolayer, this ratio seems hard to delicately control due to the uncontrollable formation of Sb vacancies. This is because the formation energy (1.86 eV) and the diffusion barrier (0.75 eV) of monovacancy-type defect in antimonene are fairly low,[2] which is difficult to trap Na^+ ions. The distribution of Na doping ratio is focused at approximately 6%, which means there is 4 Na atoms among 70 Sb atoms (approximately corresponding to our antimonene quantum dots with lateral size of ~2.5 nm). Such a relatively low defect density can ensure the structural stability of antimonene quantum dots. On the other hand, the substitutional doping of Na^+ ions can give rise to significant deformation of monolayer antimonene because of its small ionic radius,[3] if excessive, which

will induce local atomic disorder and accelerate the trend of decrystallization of antimonene. This case has occurred under a high exfoliation voltage (10 V) but does not affect the alloying process between Sb and Na atoms in thick Sb flakes because those thick flakes have enough volume to relax residual strain.

References:

(1) W. Tian, S. Zhang, C. Huo, D. Zhu, Q. Li, L. Wang, X. Ren, L. Xie, S. Guo, P. K. Chu, H. Zeng and K. Huo, *ACS Nano*, 2018, **12**, 1887-1893.

(2) X. Sun, Y. Liu, Z. Song, Y. Li, W. Wang, H. Lin, L. Wang and Y. Li, *J. Mater. Chem. C*, 2017, **5**, 4159-4166.

(3) A. Bafekry, M. Ghergherehchi and S. Farjami Shayesteh, *Phys. Chem. Chem. Phys.*, 2019, **21**, 10552-10566

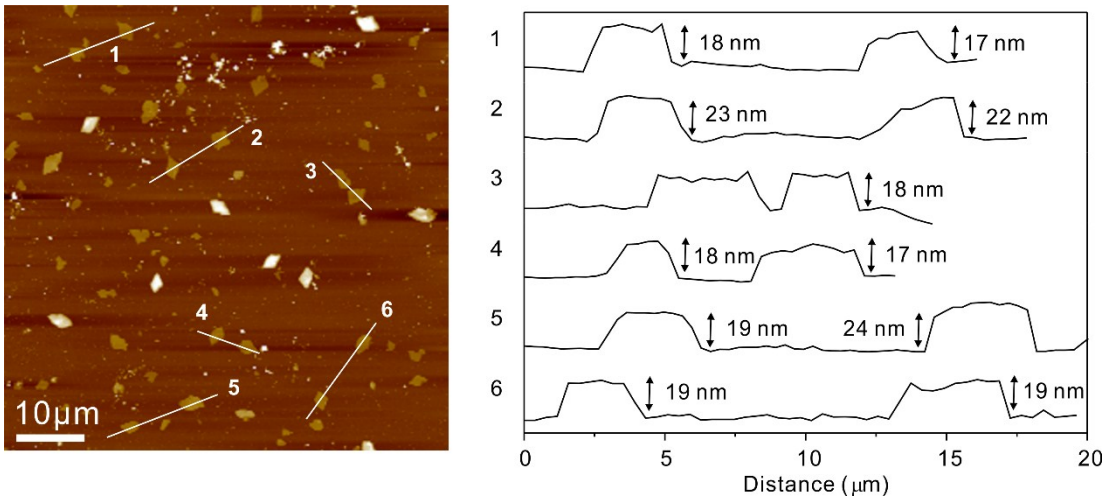

Fig. S7. AFM height image and six random selected line profiles of multi-layer Sb nanosheets located at the bottom of electrolytic cell. The average thickness and lateral size of nanosheets are ~20 nm and ~3 μm, respectively.

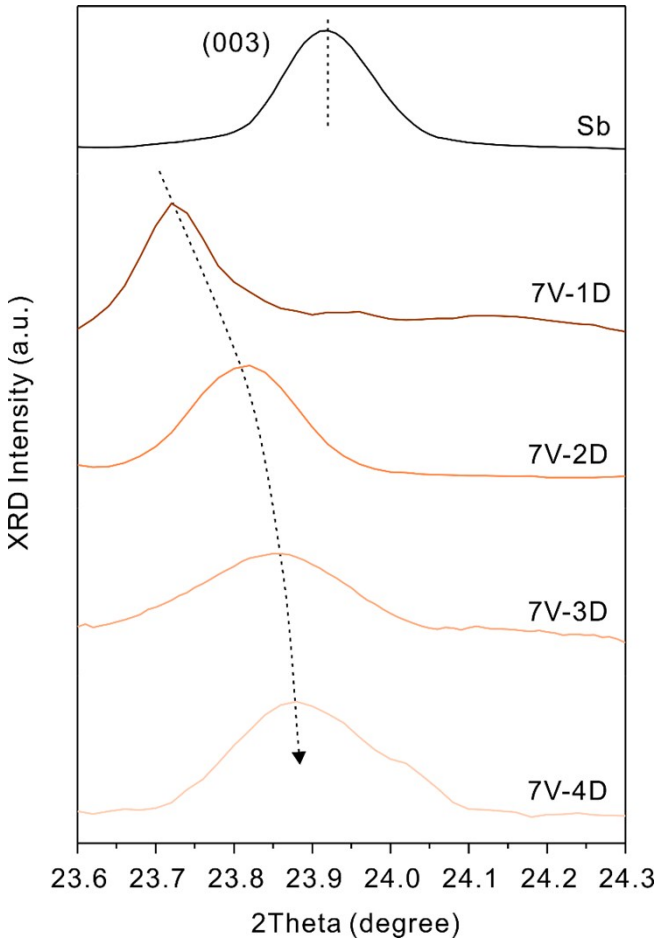

Fig. S8. XRD shift as a function of exfoliation time when the applied voltage is fixed at 7 V. Likewise, it can be seen that prolonging exfoliation time (maximum 4 days) also gives rise to a shift toward high degree direction.

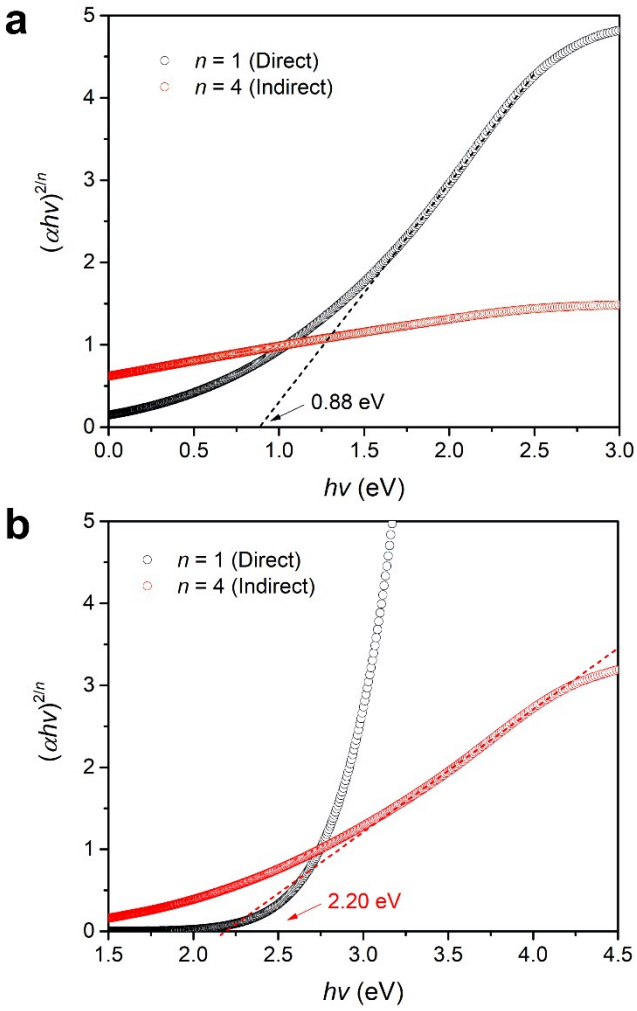

Fig. S9. Linear extrapolations on $h\nu$-axis of absorption spectra in terms of $(\alpha h\nu)^{2/n} \sim (h\nu - E_g)$, where $h\nu$ is the photon energy, A is the constant and E_g is the bandgap (0.88 eV for Sb:Na). For direct and indirect semiconductors, the value of n is 1 and 4, respectively. We have plotted two curves to perform the possible linear extrapolations on $h\nu$-axis. (a) For Na-doped antimonene, only when n = 1, the intercept on $h\nu$-axis is approximately 0.88 eV, which means this material is a direct semiconductor. (b) For pristine antimonene, n = 4 gives the bandgap value of 2.20 eV, indicating an indirect semiconductor.

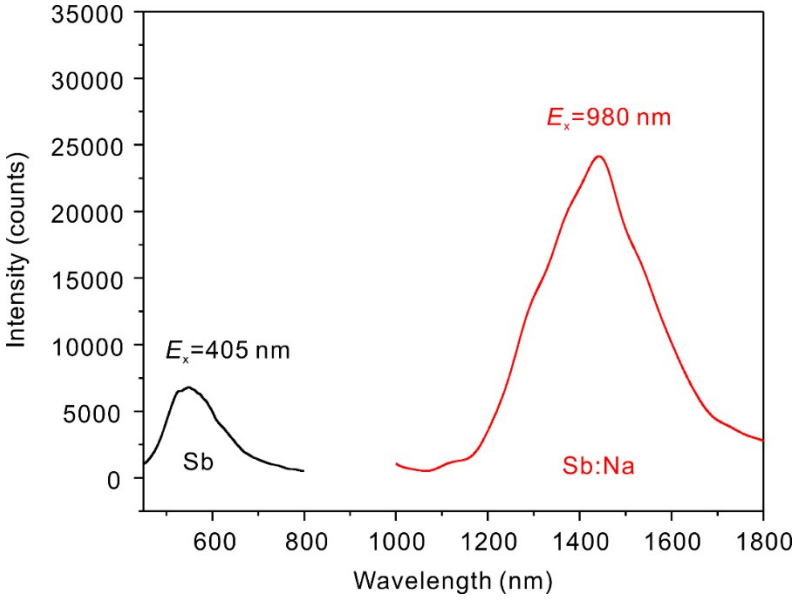

Fig. S10. PL emission comparison between monolayer Sb and Sb:Na (6%) QDs. These two emission bands are excited by 405 nm and 980 nm laser, respectively. The fluorescent intensity of Sb:Na is 4-5 times stronger than that of Sb, showing a higher efficiency of direct bandgap over indirect one.

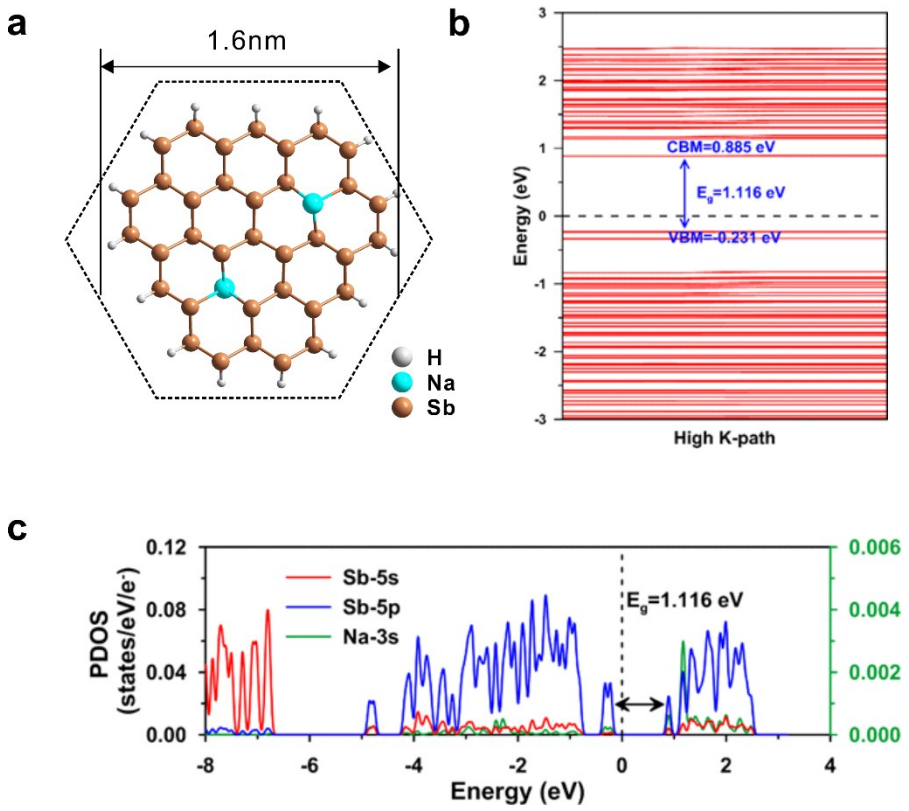

Fig. S11. First-principle calculations of Sb:Na QDs ($Sb_{35}Na_2H_{15}$). (a) Optimized crystal structure. (b) Calculated band structure. (c) Calculated projected partial density of states (PDOS).

In general, the quantization of any dimension of semiconducting materials will induce the splitting of continuous energy bands and thus broaden bandgap as the decrease of dimension (also called quantum confinement effect, QCE). For 2D quantum dot (QD) materials in the monolayer limit, more factors should be taken into account due to the further reduction of horizontal dimension. VA group elemental 2D semiconductor (e.g. phosphorene, arsenene and antimonene) QDs with sizes below 3 nm are more prone to structural deformation, which dominates over the QCE and reduces the optical gap.[1] Therefore, on the experimental aspect, the observed bandgap values for antimonene QDs are often not much blue-shifted or even red-shifted.[2-5] In addition, the surface partial oxidation (XPS in **Fig. 1(k)**) can also give rise to additional band edge states, which enhances the in-gap absorption and underestimate the gap

value.[6] This can explain why the absorption and PL spectra of Sb and Sb:Na QDs in our work have such broad linewidths (**Fig. 2(d-e)** and **Fig. S10**). Taken these two factors into account, since the characteristic radius of Sb:Na QDs is approximately 2.53 nm (below 3 nm), no significant blue-shift of optical bandgap (experiment: 0.85 eV for QD monolayer, calculation: 0.88 eV for infinite monolayer) is expected. Even so, the blue-shift of Raman spectra is evident (**Fig. 1(i)**), which indicates the QCE might contribute to the phonon behavior in our Sb:Na system.

On the theoretical aspect, to the best of our knowledge, only two papers have discussed the band structure of antimonene QDs while the majority of literature mainly focus on infinite antimonene monolayer.[1,6] These bandgap values they claimed for QDs well fill the gap of infinite monolayer in QD limit. Even so, QDs have discrete energy levels, which make it difficult to judge whether they are direct or indirect. Just like well-known silicon QD system, it is still a controversial question whether it can become direct or not.[7-8] For infinite monolayer, the band structure is continuous and we can make a quick judgement for the possible transition processes. Even though a wide range of gap values have been reported, which depend on the choice of functionals,[9] there is a consensus that the hybrid functionals that we used in this work yield a better gap determination. Therefore, to better monitor the transition of band structure, it is reasonable to consider this system as infinite one and ignore the influence of the QCE.

We have also designed a doped QD model composed by $Sb_{35}Na_2H_{15}$ (**Fig. S11(a)**, the doping level was similar to 5.55% but the size of 1.6 nm was smaller) to prove the above deduction. This fragment was passivated by hydrogen because H atoms would not contribute to photo-physics process. The generalized gradient approximation (GGA) with the Perdew-Burke-Ernzerhof (PBE) functional were used to describe the electronic exchange and correlation effects. Uniform G-centered k-points meshes with a resolution of $2\pi\times0.03$ $Å^{-1}$ and Methfessel-Paxton electronic smearing were adopted for the integration in the Brillouin zone for geometric optimization. The simulation was run with a cutoff energy of 500 eV throughout

the computations. These settings ensure convergence of the total energies to within 1 meV/atom. Structure relaxation proceeded until all forces on atoms were less than 1 meV $Å^{-1}$ and the total stress tensor was within 0.01 GPa of the target value. As depicted in **Fig. S11(b-c)**, the derived gap value is approximately 1.116 eV, which is not much blue-shifted compared with the Sb:Na infinite monolayer (0.88 eV) considering its smaller size (1.6 nm) than that of the actual size (2.53 nm). In contrast, the calculated gap value (0.88 eV) in Sb:Na infinite monolayer is closer to the experimentally-determined one (0.85 eV). Hence, these results suggest that the contribution of QCE can be offset in this doped QD system.

Reference

(1) X. Niu, Y. Yi, L. Meng, H. Shu, Y. Pu and X. a. Li, *J. Phys. Chem. C*, 2019, **123**, 25775-25780.

(2) L. Lu, X. Tang, R. Cao, L. Wu, Z. Li, G. Jing, B. Dong, S. Lu, Y. Li, Y. Xiang, J. Li, D. Fan and H. Zhang, *Adv. Opt. Mater.*, 2017, **5**, 1700301.

(3) W. Tao, X. Ji, X. Xu, M. A. Islam, Z. Li, S. Chen, P. E. Saw, H. Zhang, Z. Bharwani, Z. Guo, J. Shi and O. C. Farokhzad, *Angew. Chem. Int. Ed.*, 2017, **56**, 11896-11900.

(4) Z. Wang, R. Zhang, M. Zhao, Z. Wang, B. Wei, X. Zhang, S. Feng, H. Cao, P. Liu, Y. Hao, H. Wang, B. Xu, S. J. Pennycook and J. Guo, *J. Mater. Chem. A*, 2018, **6**, 23773-23779.

(5) C. Zhang, Y. Li, P. Zhang, M. Qiu, X. Jiang and H. Zhang, Sol. *Energy Mater. Sol. Cells*, 2019, **189**, 11-20.

(6) X. Niu, Y. Li, Y. Zhang, Z. Zhou and J. Wang, *ACS Appl. Mater. Interf.*, 2019, **11**, 17987-17993.

(7) W. D. A. M. de Boer, D. Timmerman, K. Dohnalová, I. N. Yassievich, H. Zhang, W. J. Buma and T. Gregorkiewicz, *Nat. Nanotechnol.*, 2010, **5**, 878-884.

(8) J.-W. Luo, S.-S. Li, I. Sychugov, F. Pevere, J. Linnros and A. Zunger, *Nat. Nanotechnol.*, 2017, **12**, 930-932。

(9) S. Zhang, S. Guo, Z. Chen, Y. Wang, H. Gao, J. Gómez-Herrero, P. Ares, F. Zamora, Z. Zhu and H. Zeng, *Chem. Soc. Rev.*, 2018, **47**, 982-1021

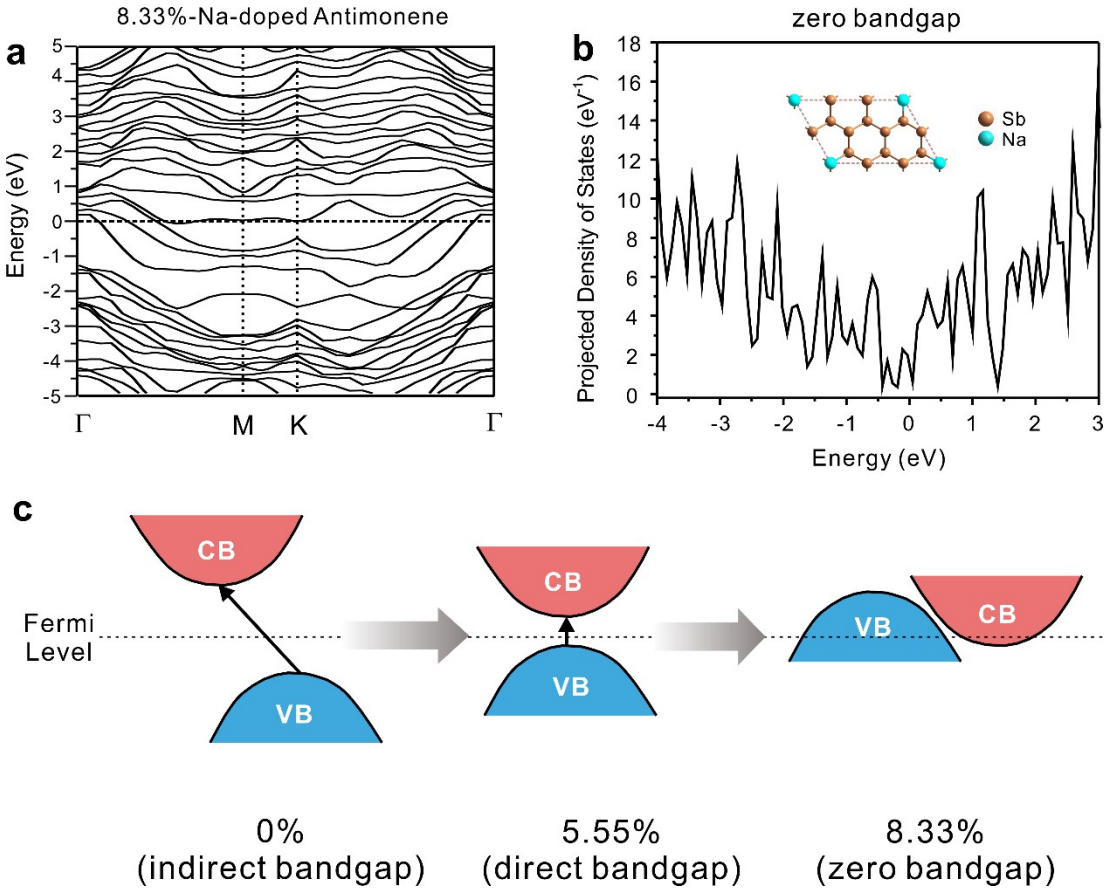

Fig. S12. Electronic band structure (a) and DOS distribution (b) of 8.33% Na-doped antimonene. Inset in (b) is the adopted 3×2×1 supercell structure. Zero dashed line denotes the Fermi level. No bandgap can be found near Fermi level and this material presents a metallic character. (c) The evolution of band structure with Na doping level.

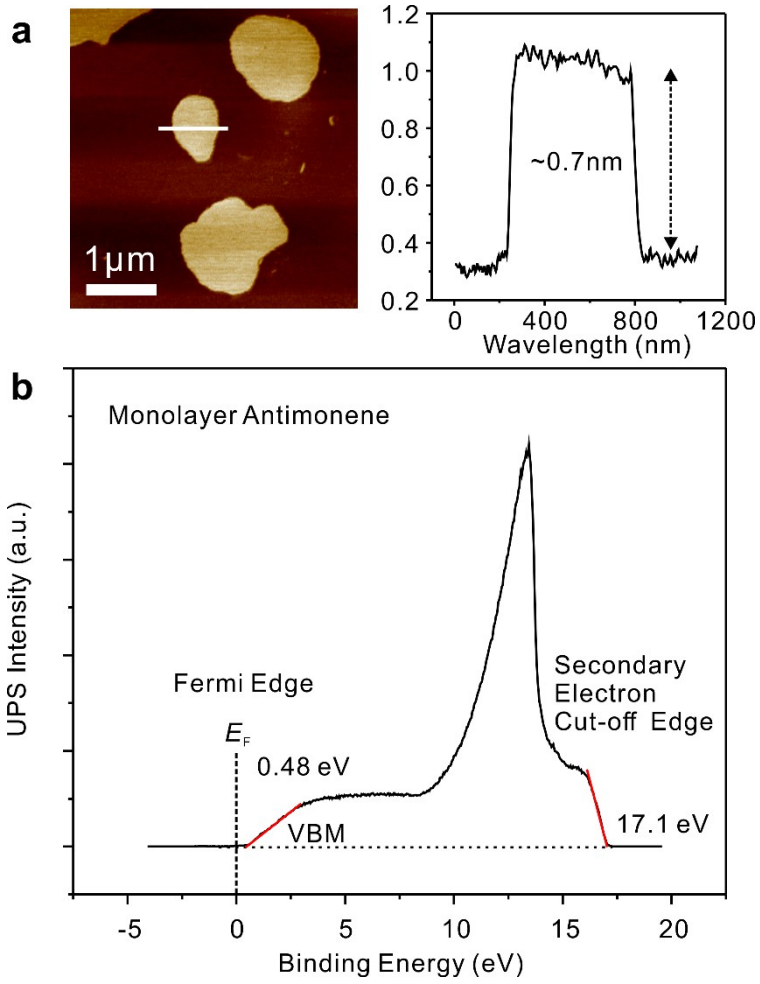

Fig. S13. AFM height image and UPS spectrum of monolayer Sb nanosheets obtained by ultrasonication method. (a) Left and right panel is AFM height picture and the corresponding line profile through a single nanosheet, respectively. The height of ~ 0.7 nm suggest the thickness of monolayer. (b) UPS spectrum from monolayer atimonene without doping. For the Fermi edge and secondary electron cut-off edge, the intercepts in energy axis can be extracted as 0.48 eV and 17.1 eV, respectively. Therefore, the E_F is located at 4.1 eV below vacuum level and the CBM and VBM positions of monolayer antimonene are determined as -2.20 eV and -4.58 eV, respectively.

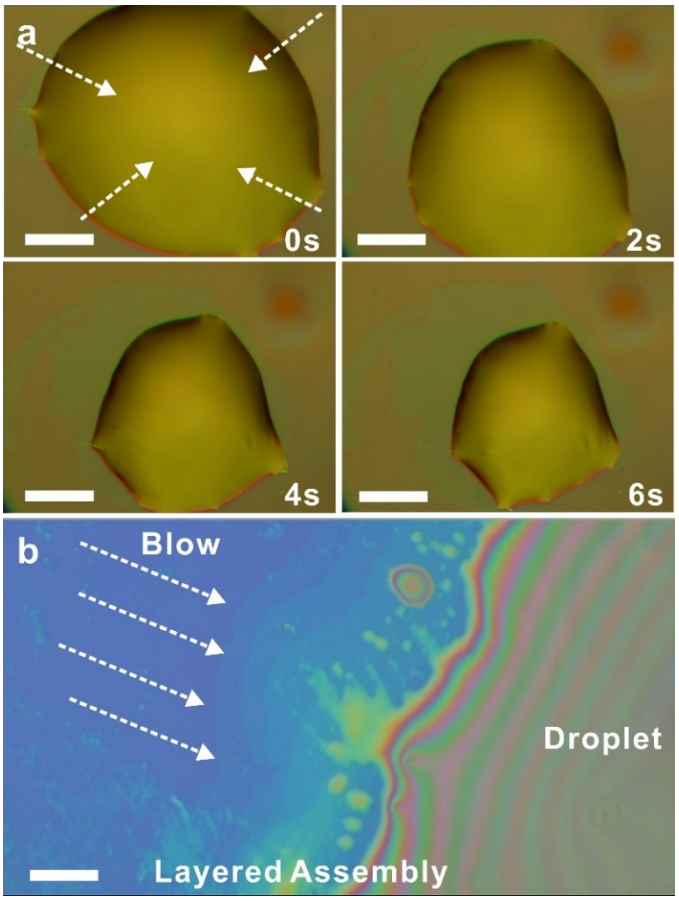

Fig. S14. Microscopic images of blow-driven self-assembly process of Sb:Na QDs. (a) A group of time-resolved film formation images with droplet evaporated. (b) Layered assembled QDs films located at the front end of droplet evaporation. The scale bars in (a) and (b) are 20 μm and 2 μm, respectively.

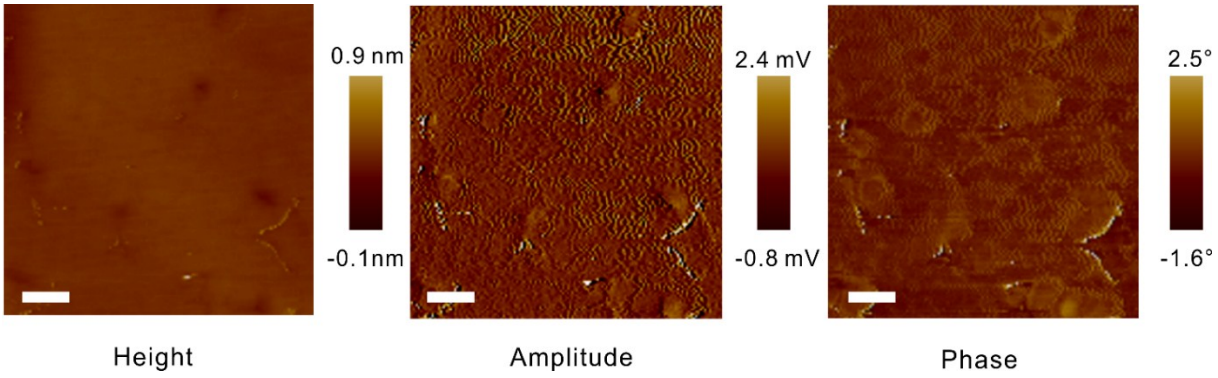

Fig. S15. AFM image of normalized assembled film. The scale bar is 50 nm. Through a vacuum drying treatment at 60°C, abnormal "disk-edge-on" stacking way can be largely eliminated and the assembled film becomes more uniform.

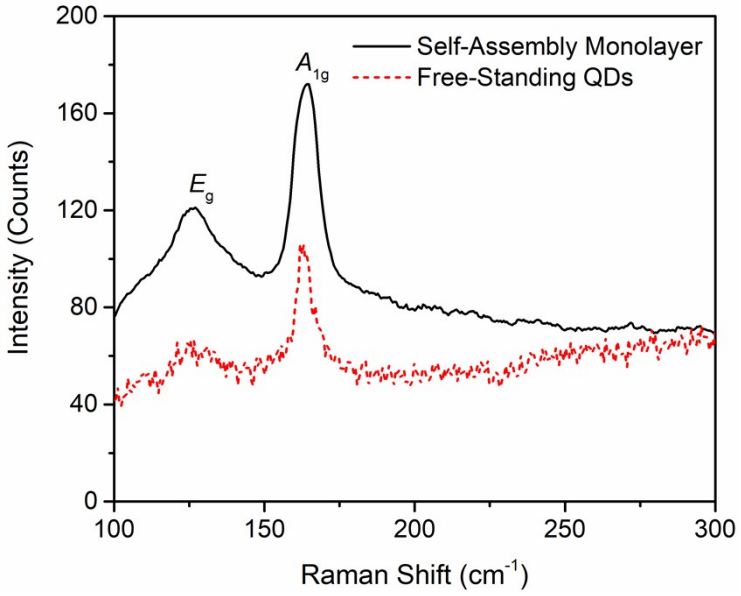

Fig. S16. The comparison of Raman spectra between self-assembly monolayer and free-standing QDs.

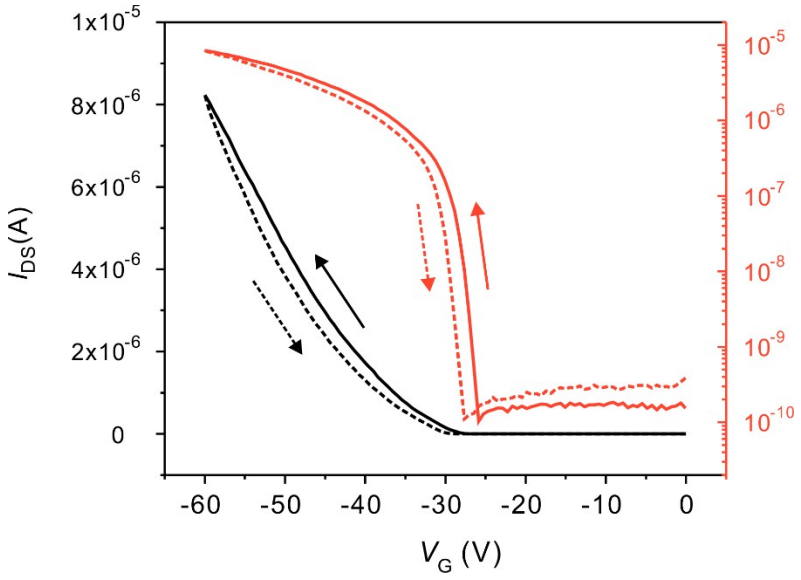

Fig. S17. Transfer characteristics and hysteresis of Sb:Na QDs FET.

As shown in **Fig. S17**, the hysteresis is defined as a threshold voltage shift between the forward and reverse sweep. A shift of approximately 2 V was observed when a sweep speed of 0.2 V/s was applied. Compared with similar FET configurations based on 2D materials,[1] this value is small, but it is still bigger than that with thin and high-*k* dielectric layer.[2-3] It is well known that further reduction of hysteresis can be achieved by changing the type of gate insulator (e.g. high-*k* Al_2O_3 and HfO_2). In addition, we have also noticed such a hysteresis has a lower back-sweep current (BSC). Martin Egginger et al. explained such a phenomenon as the traps near the interface between semiconductors and insulators.[4] In contrast, a high BSC might come from mobile ions or polarization in the dielectric materials.[4] Hence, it is reasonable to attribute the origin of our experimental results to the interface role. This is why we implemented oxygen plasma treatment for all substrates prior to spin-coating process, which can better eliminate the trap states between the QDs and the insulator.

Reference

(1) X. Jing, Y. Illarionov, E. Yalon, P. Zhou, T. Grasser, Y. Shi and M. Lanza, *Adv. Funct. Mater.*, 2019, 1901971.

(2) J. Shu, G. Wu, Y. Guo, B. Liu, X. Wei and Q. Chen, *Nanoscale*, 2016, **8**, 3049-3056.

(3) Y. Y. Illarionov, M. Waltl, G. Rzepa, J.-S. Kim, S. Kim, A. Dodabalapur, D. Akinwande and T. Grasser, *ACS Nano*, 2016, **10**, 9543-9549.

(4) M. Egginger, S. Bauer, R. Schwödiauer, H. Neugebauer and N. S. Sariciftci, *Monatsh. Chem.*, 2009, **140**, 735-750.

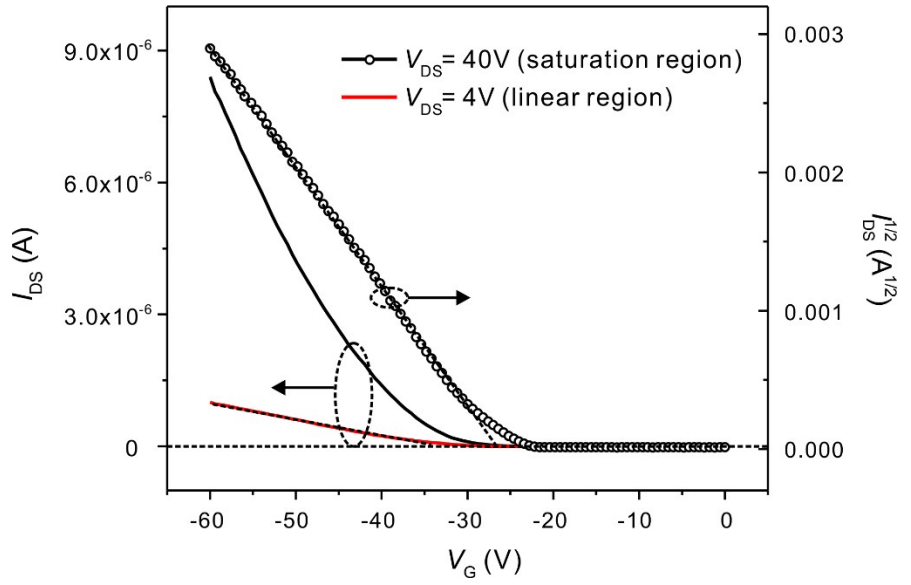

Fig. S18. Transfer characteristic curves collected from linear (V_{DS} = 4 V) and saturation (V_{DS} = 40 V) regimes.

Field-effect mobility can be divided into two categories, namely linear mobility and saturation mobility.[1-2] For the former, at a low V_{DS}, I_{DS} increases linearly with V_{DS}. Thus, the linear mobility ($\mu_{lin} = \frac{L}{WC_iV_{DS}}\frac{dI_{DS}}{dV_G}$) can be deduced by $I_{DS} = \left(\frac{W}{L}\right)\mu_{lin}C_i(V_G - V_{th})V_{DS}$ in the linear regime of transfer characteristic curve. For the latter, V_{DS} exceeds (V_G-V_{th}) and the channel is pinched off. V_{DS} will not enhance I_{DS}, and the device is said to operate in the saturation regime. In this regard, the current is given by the equation of $I_{DS} = \left(\frac{W}{2L}\right)\mu_{sat}C_i(V_G - V_{th})^2$, where μ_{sat} is the saturation mobility. In both equations, the capacitance density per unit area (C_i) can be simply descripted as $C_i = \frac{\varepsilon_0\varepsilon_r}{d}$ =1.151×10^{-8} F cm^{-2}, where ε_0 and ε_r are the vacuum permittivity (8.854×10^{-12} F m^{-1}) and the relative permittivity of SiO_2 (3.9), respectively, and d is the dielectric thickness (300 nm). When applying V_{DS} = 4 V (small enough), the device can work in the linear regime. We measured the transfer characteristic curve at this condition (red solid line in **Fig. R8**). g_m was determined as 4×10^{-8} S and thus a linear mobility μ_{lin} of 0.043 cm^{2}V^{-1}s^{-1} was obtained.

On the other hand, we can estimate the saturation mobility using the transfer characteristic curve in the saturation regime (V_{DS} = 40 V). For those black circles in **Fig. R8** corresponding to the right axis in terms of $I_{DS}^{1/2}$, the linear extrapolation on the V_G-axis can determine the threshold voltage (V_{th} = –27 V). The slope (k) is approximately –8.586×10^{-5} A$^{1/2}$ V^{-1} and therefore $\mu_{sat} = \frac{2Lk^2}{WC_i}$ =0.064 cm^{2}V^{-1}s^{-1}. This method has been widely used in the TFT electronics due to its diverse considerations.[2] For example, it can reduce the gate leakage effect. In addition, a high V_{DS} will weaken the mobility attenuation of contact resistances. The magnitude of μ_{sat} here is well consistent with that of μ_{lin}, which proves the accuracy of our mobility estimation.

Reference

(1) F. Hetsch, N. Zhao, S. V. Kershaw and A. L. Rogach, *Mater. Today*, 2013, **16**, 312-325.

(2) Y. Xu, Y. Li, S. Li, F. Balestra, G. Ghibaudo, W. Li, Y.-F. Lin, H. Sun, J. Wan, X. Wang, Y. Guo, Y. Shi and Y.-Y. Noh, Adv. Funct. Mater., 2019, 1904508.

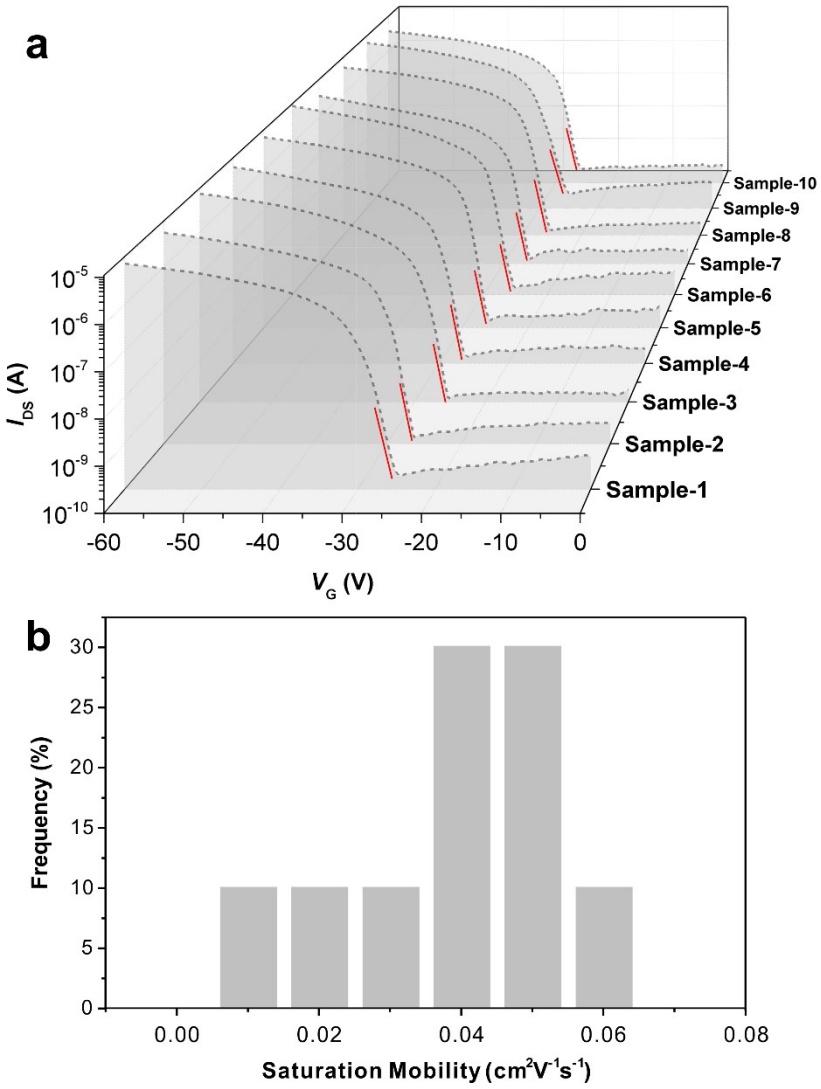

Fig. S19. Repeatability evaluation of device performance. (a) Transfer characteristic curves from ten Sb:Na based FETs working in saturation regime. Similar profiles and slopes indicate stable switching performances. (b) The statistical diagram of extracted saturation mobility values.

Table S1. Vibrational modes and molecular structure of R6G

1127 cm^{-1}	xanthene ring and $-NHC_2H_5$ group
1141 cm^{-1}	mainly C−N stretching in $-NHC_2H_5$ group
1192 cm^{-1}	xanthene/phenyl ring
1259 cm^{-1}	xanthene/phenyl ring
1307 cm^{-1}	xanthene/phenyl rings and $-NHC_2H_5$ group
1365 cm^{-1}	xanthene ring and $-NHC_2H_5$ group
1400 cm^{-1}	phenyl ring with the $-COOC_2H_5$ group
1445 cm^{-1}	phenyl ring with the $-COOC_2H_5$ group
1457 cm^{-1}	phenyl ring with the $-COOC_2H_5$ group
1488 cm^{-1}	phenyl ring with the $-COOC_2H_5$ group
1554 cm^{-1}	mainly C-C stretching in xanthene ring
1601 cm^{-1}	phenyl ring with the $-COOC_2H_5$ group
1652 cm^{-1}	xanthene ring

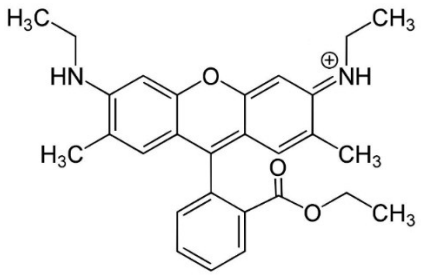

Reference

(1) H. Watanabe, N. Hayazawa, Y. Inouye and S. Kawata, *J. Phys. Chem. B*, 2005, **109**, 5012-5020

(2) P. Hildebrandt and M. Stockburger, *J. Phys. Chem.*, 1984, **88**, 5935-5944.

Note S2

Estimation of enhancement factor (*EF*): We use the Raman intensity data of bulk R6G (0.1 M R6G coated on Si/SiO_2 substrate) from Ref. 1 to calculate the *EF* [$EF=(I_{SERS}/N_{SERS})/(I_{Bulk}/N_{Bulk})$, where I_{SERS} and I_{Bulk} are the Raman intensities of SERS experiments and bulk dye molecules, respectively, and N_{SERS} and N_{Bulk} are the numbers of R6G molecules in SERS experiments and bulk dye, respectively]. All SERS signals in our measurements were collected by acquisition time of 10 seconds for 2 times. Hence, $I_{SERS}/I_{Bulk}=(20.2/20)/(630/0.4)=6.41\times10^{-4}$. Since the volume ($V_{Dye}$) and concentration ($c$) of diluted dye solution are 100 μL and 1×10^{-15} M, respectively, the area of substrate (A_{Sub}) is ~1 cm^2, the density (ρ) of bulk dye is 1.15 g cm^{-3}, laser penetration depth (h) is 21 μm, and the molar mass (M) of R6G is 479.02 g mol^{-1}, according to the reduced formula of $EF=(I_{SERS}/I_{Bulk})*(\rho hA_{Sub}/cV_{Dye}M)$, the *EF* value can be estimated to be 3.2×10^{10}.

Reference

(1) L. Tao, K. Chen, Z. Chen, C. Cong, C. Qiu, J. Chen, X. Wang, H. Chen, T. Yu, W. Xie, S. Deng and J.-B. Xu, *J. Am. Chem. Soc.*, 2018, **140**, 8696-8704

Table S2. A summary table of the enhancement factor of different 2D materials

2D Material Type	Enhancement Factor (EF) or Limit of Detection (LOD) for R6G	Reference
Li/Na Intercalated 1T-MoS_2	EF: 2.92×10^4	*Chem. Mater.* **2019**, *31*, 5725-5734.
Mechanically-Exfoliated 1T'-WTe_2	EF: 1.8×10^9	*J. Am. Chem. Soc.* **2018**, *140*, 8696-8704.
Mechanically-Exfoliated 1T'-$MoTe_2$	EF: 1.6×10^8	
PECVD Derived Graphene QDs	LOD: 10^{-9} M	*Nat. Commun.* **2018**, *9*, 193
Oxygen-Incorporated MoS_2	LOD: 10^{-7} M	*Nat. Commun.* **2017**, *8*, 1993.
Graphene/Au	EF: 10^{10}; LOD: 10^{-14} M	*Adv. Mater.* **2013**, *25*, 4918-4924.
Ti_2N Nanosheets	EF: 10^{12}	*ACS Nano* **2017**, *11*, 8892-8900.
MoO_2 Nanosheets	EF: 2.1×10^5; LOD: 4×10^{-8} M	*Small*, **2018**, *14*, 1802276.
1T'-ReS_2 Nanosheets	LOD: 10^{-9} M	*Small* **2018**, *14*, 1704079
$Ti_3C_2T_x$ MXenes	EF: 10^6	*J. Phys. Chem. C* **2017**, *121*, 19983-19988.
1T-$MoSe_2$	LOD: 10^{-8} M	*Adv. Funct. Mater.* **2017**, *27*, 1606694.
WSe_2	Exceeding graphene by a factor of 2	*Chem. Mater.* **2016**, *28*, 180-187.
BN/Au	LOD: 10^{-9} M	*ACS Nano* **2016**, *10*, 11156-11162.
Sb:Na Quantum Dots	**EF: 3.2×10^{10}; LOD: 10^{-16} M**	**This work**

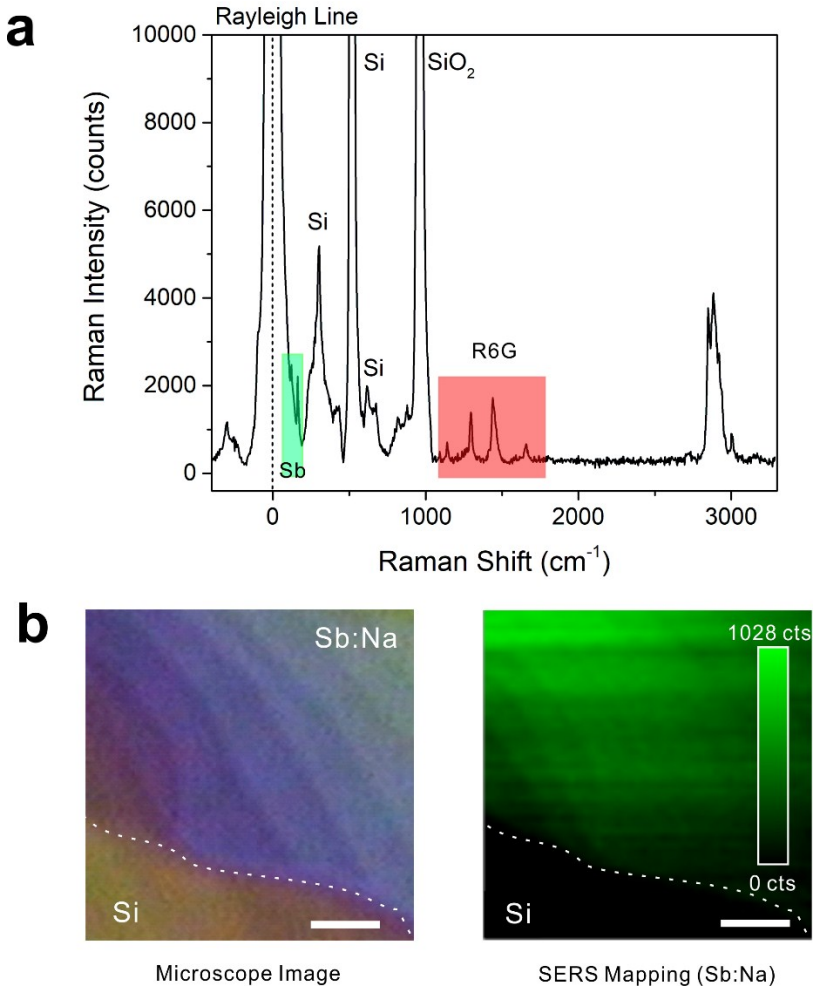

Fig. S20. (a) A typical survey Raman spectrum from Sb:Na/R6G supported on Si/SiO_2 substrate. Green and red boxes indicate characteristic Sb and R6G Raman peaks, respectively. These two bands are adopted to collected Raman mapping of Sb QDs and R6G molecules. (b) Layered structure image (left panel) and Raman mapping image of assembled Sb:Na QDs on Si/SiO_2 substrate. The scale bar is 1 μm.

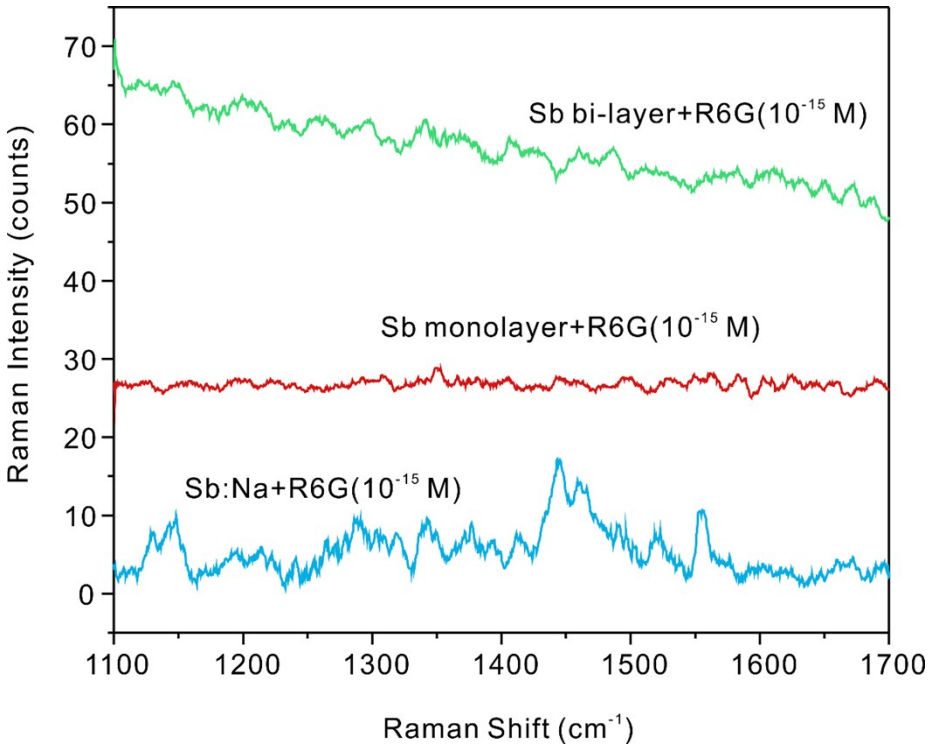

Fig. S21. Raman spectra from different antimonene-based substrates capped by R6G molecules with concentration of ≈1×10^{-15} M. A more obvious Raman fine structure of R6G molecules can be observed on the Sb:Na QD substrate.

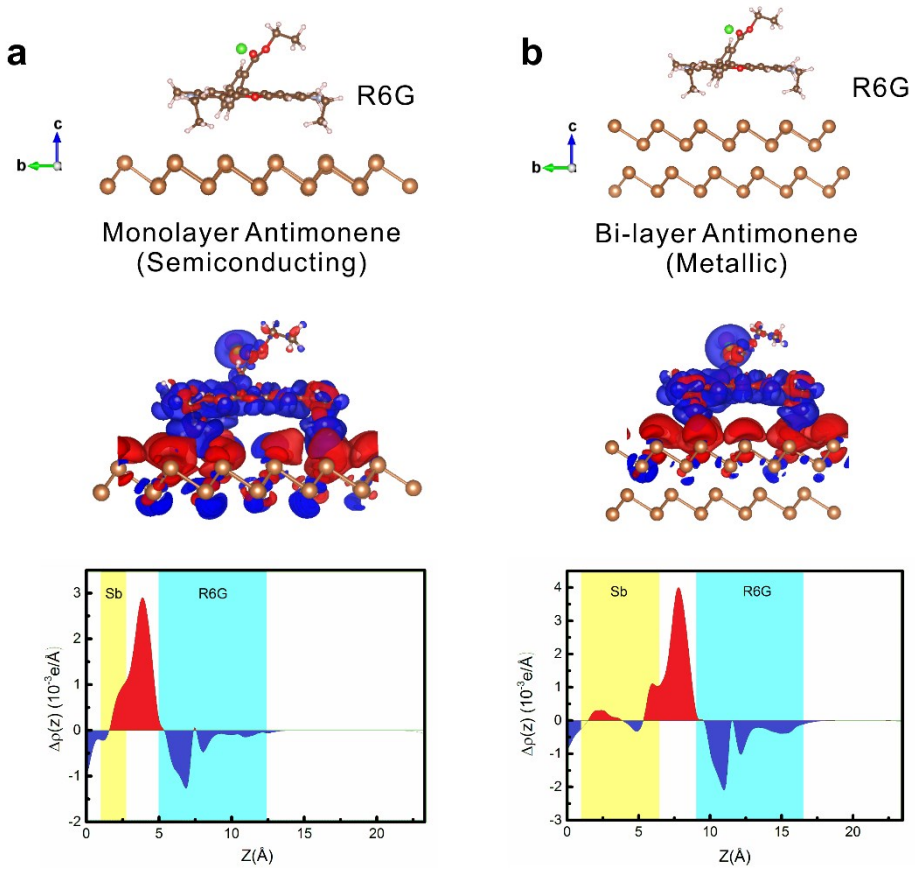

Fig. S22. 3D charge density distribution and charge density difference plot of R6G molecules with monolayer (a) and bi-layer (b) antimonene. It can be seen that those transferred electrons are mainly accumulated between antimonene and R6G molecule, which might form interface dipoles that contribute to the SERS process.

Table S3. Binding energies in three calculated configurations

Configuration	Sb Energy (eV)	R6G Energy (eV)	Total Energy (eV)	Binding Energy (eV)
R6G/monolayer antimonene	−213.73 eV	−407.59 eV	−622.17 eV	0.85 eV
R6G/bi-layer antimonene	−436.98 eV	−407.59 eV	−845.46 eV	0.89 eV
R6G/Sb:Na	−210.08 eV	−407.59 eV	−618.74 eV	1.07 eV

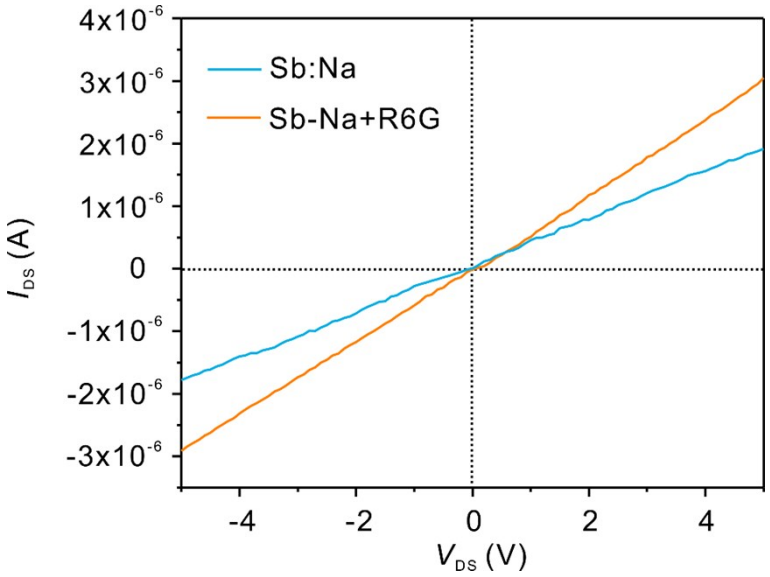

Fig. S23. Current-voltage characteristics of Sb:Na based FET device (V_G = -50V) before and after the addition of R6G molecules (≈1×10^{-15} M). The obvious increase of I_{DS} after R6G capping demonstrates an effective electron injection from R6G to Sb:Na.

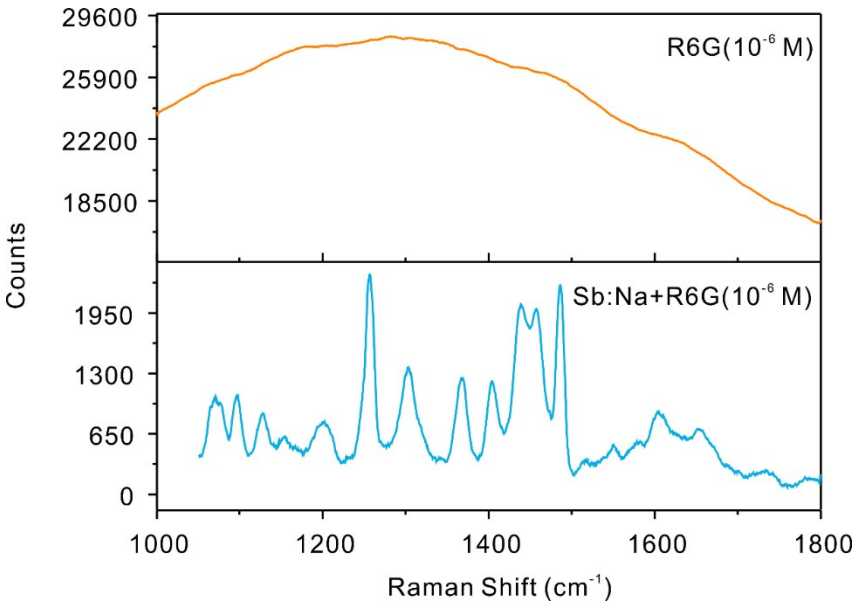

Fig. S24. Raman spectra from R6G molecules with concentration of ≈1×10^{-6} M dispersed on silicon substrate and Sb:Na QDs substrate. A broad PL emission band of R6G can be totally suppressed when they are supported on Sb:Na QDs substrate, indicating an effective charge separation process at Sb:Na/R6G interface.

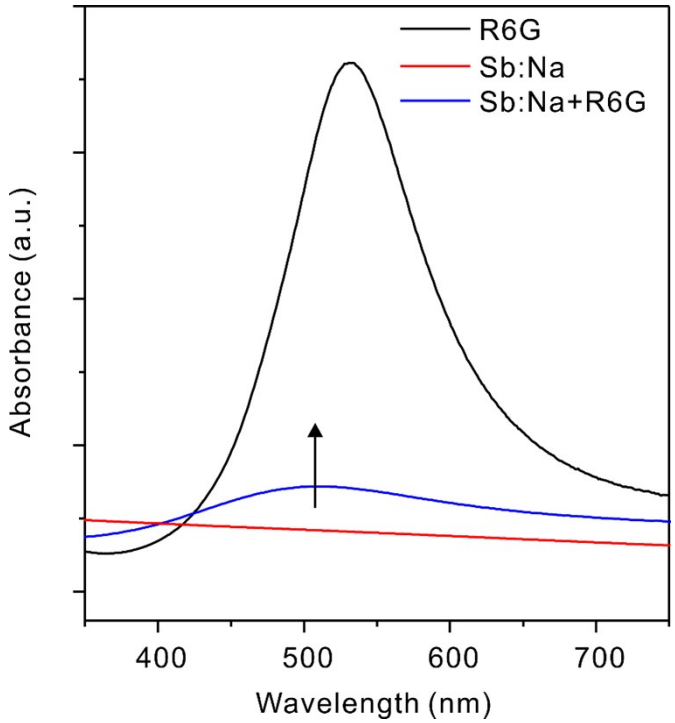

Fig. S25. UV-visible spectral comparison among R6G (≈1×10^{-6} M), Sb:Na, and Sb:Na/R6G. The original reflectance (R) experimental data are converted to absorbance (A) by the Kubelka-Munk formula [$A = (1-R)^2/2R$]. An evident absorption band with peak at ~ 510 nm emerges, which is closely correlated with the absorption of charge transfer complex and indicative of underlying chemical enhancement mechanism for Sb:Na-based SERS process.

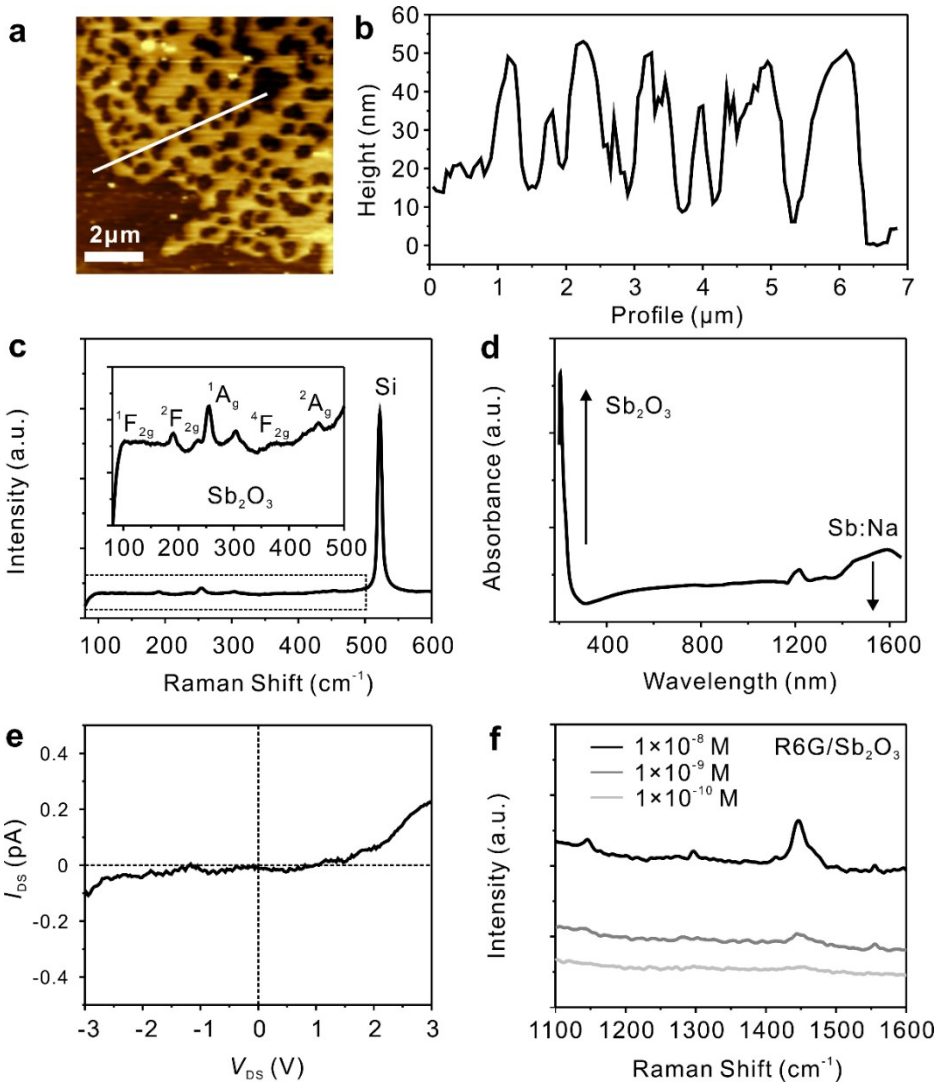

Fig. S26. Characterizations and measurements of antimonene oxide. (a) AFM image and (b) the corresponding height profile. (c) Raman spectrum. (d) Absorption spectrum. (e) *I-V* curve. (f) SERS effect with different concentrations of R6G on Sb_2O_3.

Referenced by previous report,[1] we put the assembled Sb:Na QDs film supported on Si/SiO_2 substrate onto a hot plate at a temperature of 400°C for 1 min. As shown in **Fig. S24(a-b)**, after the thermal oxidation process, continuous and dense QDs film becomes porous and rough. According to Raman spectral measurements (**Fig. S24(c)**), the phase is determined as α-Sb_2O_3.[2] The formation of porous topology is most likely due to their structural mismatch (α-Sb_2O_3:

cubic, β-Sb: rhombohedral). Moreover, with the transformation of structure, the original IR absorption band of Sb:Na decreases too much and a newly-formed ultraviolet absorption edge can be found in **Fig. S24(d)**. Such a change corresponds to the formation of wide bandgap α-Sb_2O_3 phase and its bandgap value accords with some theoretical and experimental results.[2-3] We have further measured the *I-V* characteristics of α-Sb_2O_3 film (**Fig. S24(e)**), which indicates that it is highly-resistive (resistivity increases by three orders of magnitude at 3V compared with the Sb:Na film) and cannot be driven by the field effect. Finally, we have attempted to test the SERS activity of α-Sb_2O_3 for R6G molecules. As shown in **Fig. S24(f)**, despite of a certain degree of enhancement, the limit of detection just maintains to be about 1×10^{-10} M, which is far below the level of Sb:Na. Since α-Sb_2O_3 is an indirect band structure,[2] the efficiency of PICT process is limited.

Reference

(1) Q. Wu and Y. J. Song, *Chem. Commun.*, 2018, **54**, 9671-9674.

(2) W. Han, P. Huang, L. Li, F. Wang, P. Luo, K. Liu, X. Zhou, H. Li, X. Zhang, Y. Cui and T. Zhai, *Nat. Commun.*, 2019, **10**, 4728.

(3) Q. Wu, T. Jeong, S. Park, J. Sun, H. Kang, T. Yoon and Y. J. Song, *Chem. Commun.*, 2019, **55**, 2473-2476.